New Journal of Physics
The open access journal for physics

Bow-tie nano-antenna assisted generation of extreme ultraviolet radiation

N Pfullmann[1,2,6], C Waltermann[1,2], M Noack[1,2], S Rausch[1,2], T Nagy[1,2], C Reinhardt[1,2], M Kovačev[1,2], V Knittel[3], R Bratschitsch[4], D Akemeier[5], A Hütten[5], A Leitenstorfer[3] and U Morgner[1,2]

[1] Leibniz Universität Hannover, Institut für Quantenoptik, Welfengarten 1, D-30167 Hannover, Germany
[2] QUEST, Centre for Quantum Engineering and Space-Time Research, Hannover, Germany
[3] Department of Physics and Center for Applied Photonics, University of Konstanz, D-78457 Konstanz, Germany
[4] Technische Universität Chemnitz, Institut für Physik, Dynamik Nanoskopischer und Mesoskopischer Strukturen, D-09107 Chemnitz, Germany
[5] Thin Films and Physics of Nanostructures, Department of Physics, Bielefeld University, D-35501 Bielefeld, Germany
E-mail: pfullmann@iqo.uni-hannover.de

New Journal of Physics **15** (2013) 093027 (14pp)
Received 1 April 2013
Published 17 September 2013
Online at http://www.njp.org/
doi:10.1088/1367-2630/15/9/093027

Abstract. We report on the generation of extreme ultraviolet radiation utilizing the plasmonic field enhancement in arrays of bow-tie gold optical antennae. Furthermore, their suitability to support high-order harmonic generation is examined by means of finite-difference time-domain calculations and experiments. Particular emphasis is paid to the thermal properties, which become significant at the employed peak intensities. A damage threshold depending on the antenna length is predicted and confirmed by our experimental findings. Moreover, the gas density in the vicinity of the antennae is characterized experimentally to determine the number of atoms contributing to the measured radiation, which is almost an order of magnitude larger than previously reported.

[6] Author to whom any correspondence should be addressed.

Contents

1. Introduction

For radio frequencies and in the microwave regime, antennae are widely used for various applications. In the visible spectral range however, the concept has only recently been introduced [1]. Optical antennae offer a wide range of applications though, spanning from the extreme concentration and manipulation of light [2], nonlinear optics [3, 4] to the generation of high-order harmonic radiation [5]. This process is of particular interest because it paves the way for experiments on attosecond time-scales [6], e.g. among other things, new measurements in fundamental physics to study electron dynamics in molecules [7]. Moreover, it enables the extension of the frequency comb technique [8] in high-precision spectroscopy to the extreme ultraviolet (EUV) regime [9]. This extension is challenging though, due to the low conversion efficiency of the high-order harmonic generation (HHG)-process in combination with the pulse energies available from few-cycle femtosecond oscillators. In order to mitigate these issues external enhancement cavities have been developed and investigated extensively [10–13].

By employing a plasmonic resonance in optical nano-antennae, an compelling alternative approach for HHG directly from a laser oscillator has been proposed by Kim *et al* [5]. Theoretical investigations of the scheme have revealed many interesting phenomena like even-order harmonics [14, 15], which are triggered by the occurring steep near-field gradients. Based on a different antenna geometry even the generation of attosecond pulses [16] is predicted. Experimentally however, the scheme is challenging to implement and atomic line emission (ALE) alone instead of HHG has been reported in a similar experimental setup [17]. Recently Park *et al* [18] have published new results and provided experimental details to clarify the origin of the observed EUV radiation. As pointed out by Raschke [19] further experiments are necessary to resolve this open question, though.

Here, we present a detailed analysis of bow-tie optical antennae with respect to their suitability to support HHG. Particular attention is paid to the thermal properties, which become significant at the peak intensities necessary for HHG. By means of a theoretical model and finite-difference time-domain (FDTD) calculations, we are able to explain the experimental findings, giving rise for future improvements. Moreover, the number of atoms contributing to the measured EUV spectrum is determined experimentally to get a better insight into the involved processes. For theoretical considerations of the generated spectra we refer to the respective literature looking into different aspects of HHG driven by plasmonic fields [20–28].

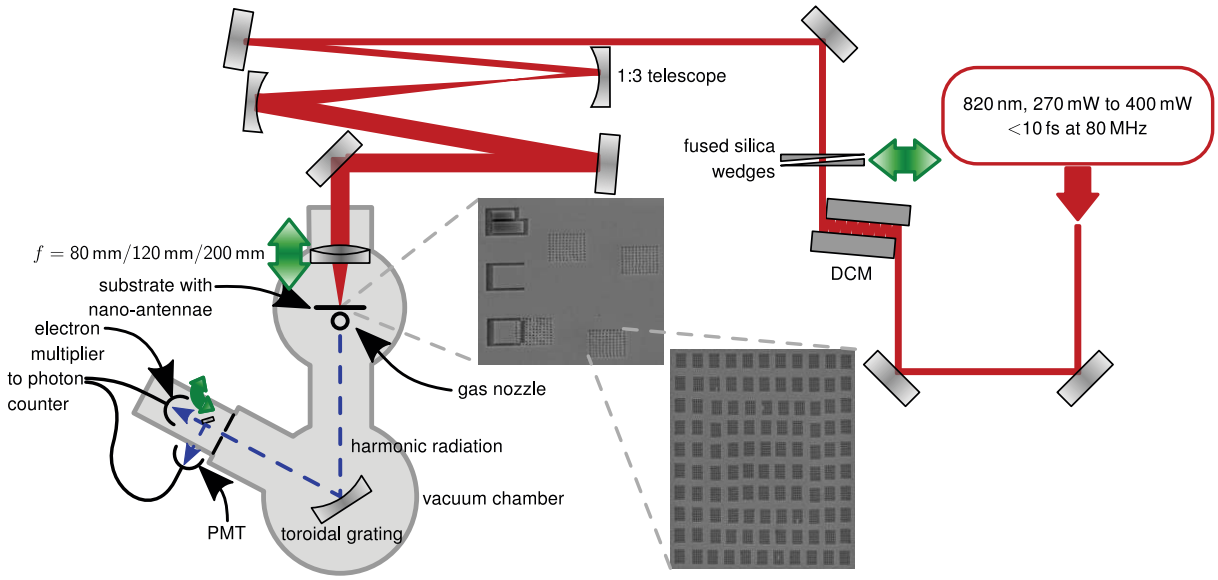

Figure 1. Experimental set-up. Laser pulses from a Ti:sapphire oscillator are focused by an achromatic lens onto arrays of optical antennae. Low harmonic orders are generated and analysed with different detectors (see text for details).

2. Experimental set-up

Figure 1 depicts the experimental set-up, which is analogous to the one used in previous experiments on low order harmonic generation with gold nano-rods as optical antennae [29]. A Ti:sapphire oscillator (Venteon, Pulse one) delivers pulses with a pulse duration of <10 fs and a pulse energy of up to 5 nJ centred at 820 nm. The pulses are negatively chirped by several bounces on dispersive mirrors to compensate for dispersion added later, i.e. a vacuum window, an achromatic lens and the substrate. The dispersion is fine-tuned via a pair of thin fused silica wedges. Finally, a telescope with a ratio of one to three expands the beam size to enable tight focusing with a variety of achromatic lenses. The lens is mounted on a translation stage to adjust the focal position as indicated by the green arrow, without breaking the vacuum. The focal spot size ranges from 20.6×13.8 to $8.2 \times 5.6\,\mu$m with corresponding peak intensities of 2×10^{11}–13×10^{11} W cm^{-2}, respectively. The sample with the nano antennae is attached to a second translation stage moving in x- and y-direction to selectively address different antenna arrays, which appear as squares in the SEM image in figure 1 due to their extremely high packing density. The laser polarization and the antenna axis are aligned parallel to each other. To efficiently detect the generated EUV radiation a confocal monochromator setup (modified McPherson 234/302, 1200 lines mm^{-1} grating for 110–310 nm, 2400 lines mm^{-1} grating for 20–110 nm) is used, where the generation volume acts as an entrance slit. The sample is thus mounted in the focal point of the toroidal mirror and the photon collection efficiency is maximized [30, 31]. Finally, a photo multiplier (PMT) capable of single photon counting (Hamamatsu H8259-09) is used in combination with a photon counter (Scientific Research SR400) to measure the third harmonic signal behind the exit slit. By flipping a mirror into the harmonic beam and setting the monochromator to the appropriate wavelength, it is possible to easily switch between signal detection for the third harmonic and EUV radiation. The latter

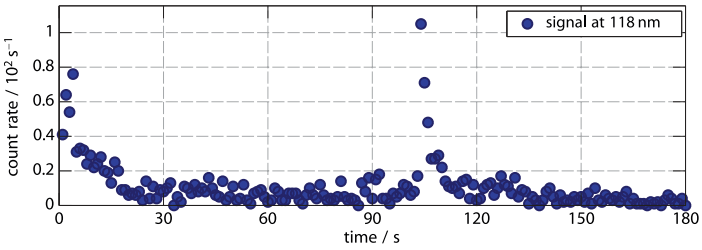

Figure 2. Harmonic signal in dependence of illumination time. The signal drops exponentially and stabilizes at a significantly reduced level. After approximately 100 s the sample was slightly translated to illuminate a fresh spot within the antenna array leading to a temporary signal increase. This points to an initial change of the original antenna structure, which is not altered further.

is detected with an electron multiplier (Photonis 4751G) in combination with a pre amplifier (Minicircuits ZFL 500LN+) instead of the PMT.

The pulse duration of the incident laser pulses was measured with an interferometric autocorrelator (Venteon, Pulse four IAC) as well as a SPIDER setup (Venteon, Pulse four SPIDER) at the position of the sample to check the dispersion control and verify the expected pulse duration of < 10 fs.

The bow-tie shaped gold nano-antennae are manufactured with focused ion beam (FIB) milling on sapphire substrates with a thin chromium layer underneath to serve as an adhesion layer. The antennae have a length from 140 nm up to 200 nm with an opening angle of 30° and a thickness of 50 nm and a nominal gap size of 20 nm. The arrays have a quadratic shape with an edge length of 10 μm as can be seen in the SEM image inset in figure 1. A detailed SEM picture of the antennae prior to illumination with the laser beam is shown in figure 3(a).

To observe EUV radiation gas is fed onto the sample through a homebuilt glass nozzle with a diameter of 50 μm. The gas nozzle is mounted on a xyz-stage to optimally align the gas jet onto the laser focus. Furthermore, a mass flow controller (MKS 647C controller) is used to ensure a constant gas pressure at the sample during the experiments. Details concerning the gas distribution behind the nozzle are discussed in section 5. With the gas flow turned on the background pressure is at around 1×10^{-4} and 1×10^{-6} mbar without gas flow, respectively.

We use the plasmonic enhanced third harmonic from the nano-antennae to optimize the focal position as well as the alignment of the antenna array relative to the laser focus.

3. Experimental results

Similar to our previous experiments with rod-type optical antennae [29] we observe a rapid destruction of the samples, which has recently also been reported by Park *et al* [18, 32]. With xenon gas flow turned on, we measure the highest photon numbers at 118 nm, which is thus used to further characterize the antennae. Figure 2 shows the measured radiation at 118 nm as a function of the illumination time. We observe an exponential decrease of the generated radiation, which saturates at about 10% of its initial value and increases again after translating the sample to illuminate a fresh spot within the antenna array (after approximately 100 s). Thus the original antenna design is presumably first changed due to thermal reshaping and then remains in a different shape without further changes [33]. Despite the substantial decrease, the remaining

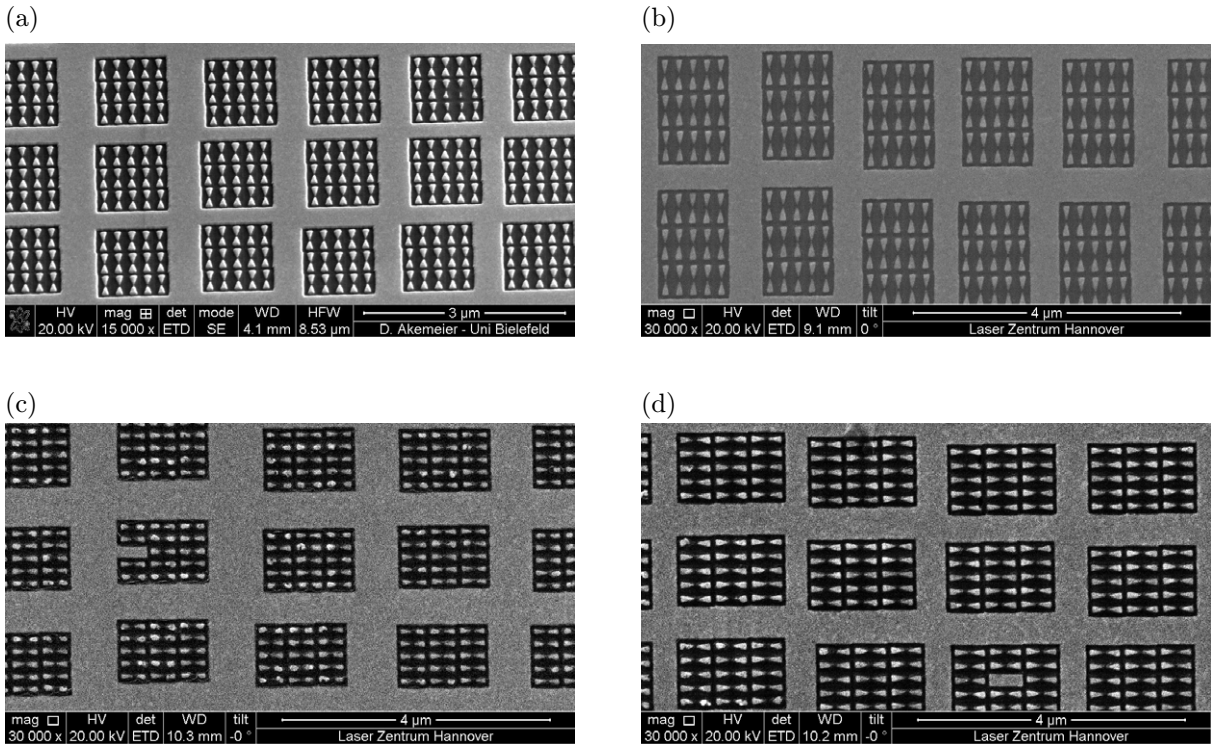

Figure 3. (a), (b) Bow-tie antennae before and after illumination (with a peak intensity of 2×10^{11} and 6×10^{11} W cm^{-2}) with varying antenna arm lengths and different achromatic lenses used to focus the laser beam. Only above an intensity threshold antenna destruction is observed (c). Additionally the destruction strongly depends on the antenna arm length since 140 nm long antennae (with a peak intensity of 13×10^{11} W cm^{-2}) are widely damaged (c), whereas only a few 200 nm long antennae (with a peak intensity of 13×10^{11} W cm^{-2}) are changed (d).

enhancement of the nano-antennae is still sufficient to support the generation of radiation at 118 nm. To assess the reshaping process, SEM images are taken before and after laser pulse illumination, which are discussed below.

The decrease of the harmonic signal is caused by melting of the nano-antennae as depicted in the SEM images in figure 3. Figure 3(a) shows the antennae prior to laser illumination with clearly identifiable bow-tie optical antennae separated by a gap. At a peak intensity of approximately 6×10^{11} W cm^{-2} no antenna damage is observed as shown in figure 3(b). For the highest available peak intensity however, antenna damage is found depending on the antenna length as depicted in figures 3(c) and (d). At an antenna length of 140 nm regular antenna damage due to melting is found, whereas only occasional damage is present for longer antennae with a length of 200 nm. The melting leads to a significantly increased gap size and hence a reduced electric field enhancement. Consequently, the nonlinear signal is also reduced as plotted in figure 2.

At a higher magnification of the SEM images antenna destruction becomes even clearer and additional information is obtained by using different detectors to examine backscattered

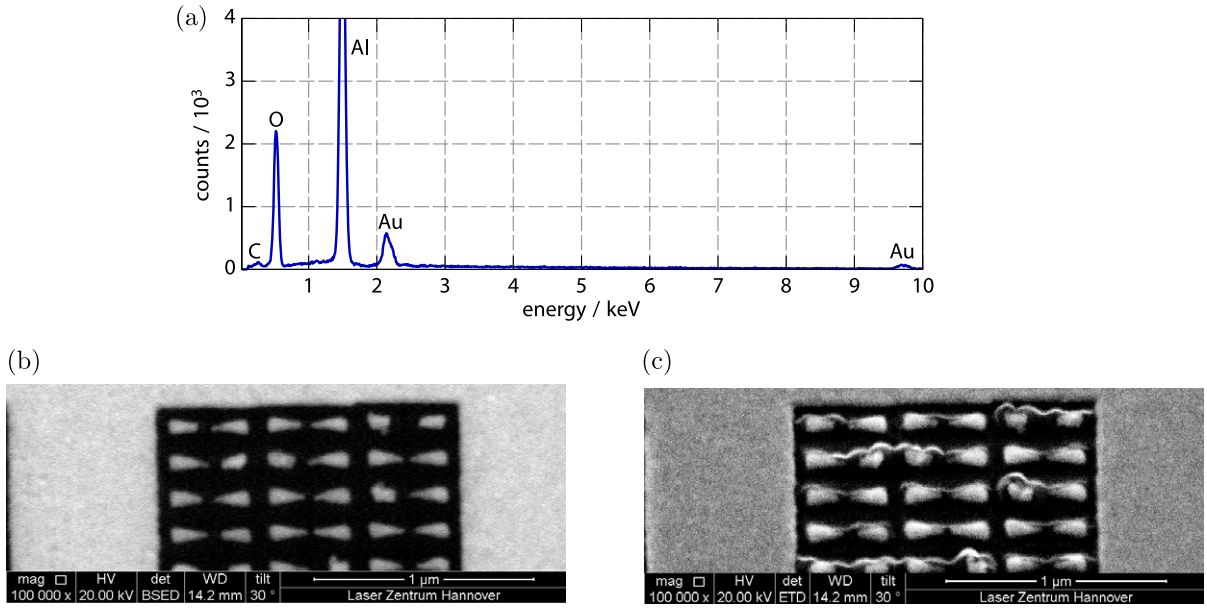

Figure 4. SEM analysis of damaged antennae with different detectors and energy-dispersive x-ray spectroscopy. According to spectrum (a) no contamination is present in the analysed area, while from (b) the destroyed antennae are clearly visible. Panel (c) reveals information about the sample's topology and points towards a damaged substrate material.

or secondary electrons in the SEM images in figure 4. Due to the backscattered electrons used in figure 4(b) the bright areas represent gold, whereas the dark areas correspond to the substrate material. Secondary electrons in figure 4(c) on the other hand not only contain information about the material, but also reveal the sample's topography, which is clearly non-uniform in close proximity to the antennae, although the adjacent substrate material is not altered. Additional information about the chemical compounds in the analysed area is gained by energy-dispersive x-ray spectroscopy, with the respective spectrum plotted in figure 4(a). It only contains measurable peaks for gold, aluminium, oxygen and carbon. The latter is likely caused by handling the sample outside a sealed atmosphere and is low in comparison with the others. Most prominent are the peaks form aluminium and oxygen, which result from sapphire as a substrate material. Since the antennae only comprise a small part of the analysed area, the peaks resulting from gold are also low compared with those from e.g. oxygen. Most importantly no other peaks occur and sample contamination is ruled out as a source for the incongruities in the secondary electron picture. For sapphire optical breakdown with subsequent shape changes has been observed previously at a threshold intensity of $1.4(4) \times 10^{13}\,\mathrm{W\,cm^{-2}}$ [34]. Based on our simulations described in the following, these intensities are experimentally feasible in the vicinity of the antennae. The incongruities are therefore most likely caused by a damaged substrate material, resulting in a final topography shown in figure 4(c). Moreover, the simulations also reveal a damage threshold depending on the antenna length, which has been found experimentally.

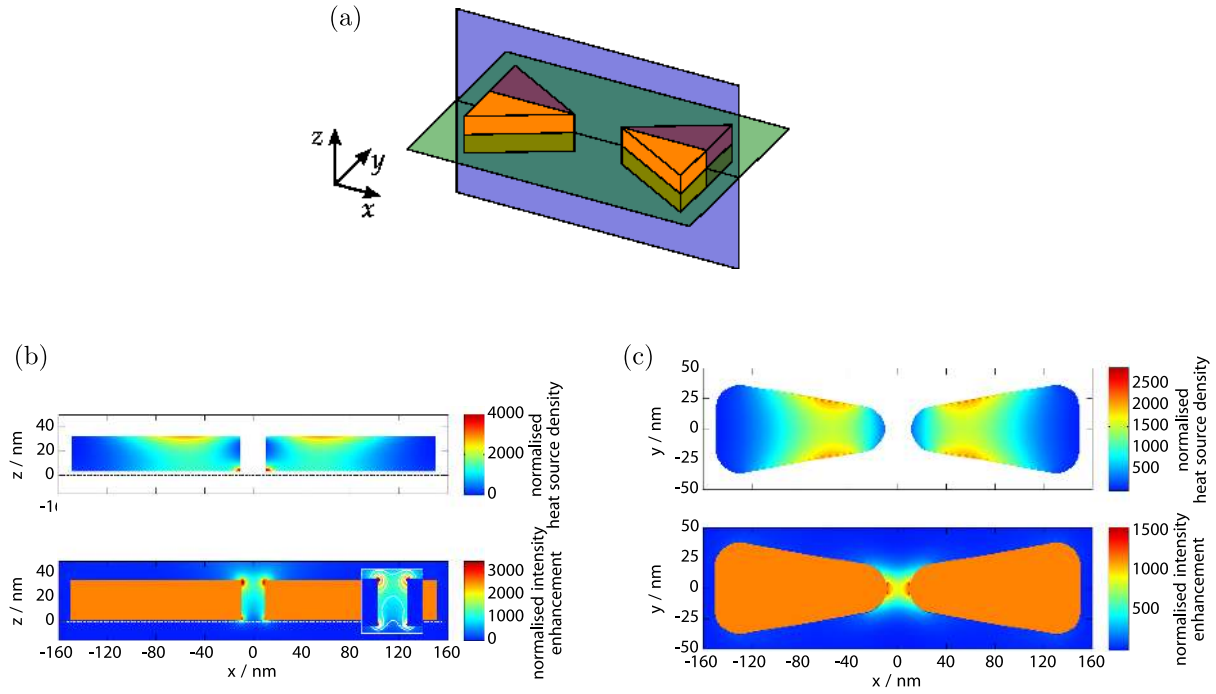

Figure 5. Top: heat source density of a bow-tie antenna with 140 nm antenna length, 30° opening angle, 20 nm feed gap, 20 nm radius of curvature and an antenna height of 30 nm. Bottom: corresponding normalized intensity enhancement. (a) Analysis planes and (b) heat source density in yz-plane. Dashed lines indicate the surface of the substrate, (c) heat source density in xy-plane.

4. Numerical methods

To simulate the response of the antennae to an ultrashort laser pulse the freely available FDTD code MEEP [35] is employed. Periodic boundary conditions in x- and y-direction mimic the antenna array used experimentally and perfectly matched layers in z-direction avoid numerical reflections of the incident field. The parameters to model the dispersive behaviour of gold are taken from [36], whereas all other parameters are taken from the experiment. The temperature distribution within the antennae is given by the heat source density [37] and plotted together with the normalized intensity enhancement in figure 5 both in the xy- and the xz-plane for a bow-tie antenna with 140 nm antenna length. In figure 5(b) the substrate is located in the bottom half of both plots and treated as an ideal dielectric with a zero imaginary part of the dielectric function. Thus, the heat source density is also zero and the laser pulse itself does not deposit heat in the substrate. The substrate is therefore only heated via heat conduction and serves as a cooler for the antenna.

In the antenna on the other hand, the non-zero imaginary part of the dielectric function leads to heating of the structure with two prominent maxima in each antenna arm. One occurs at the apex' bottom caused by the strong local electric field there, which also reaches into the antenna material. The other one is located at the top of the antenna at the interface to the surrounding dielectric, i.e. vacuum or air. Its origin becomes clearer after examining the electric field in

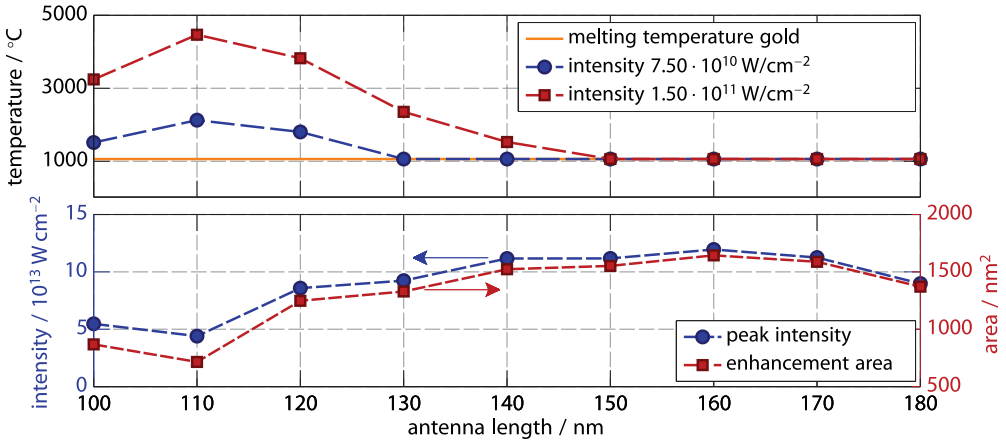

Figure 6. Maximal antenna temperature for different incident intensities as a function of the antenna length L and temperature optimization of bow-tie nano-antennae. The given peak intensity includes the incident intensity and the enhancement exhibited by the antennae.

the xy-plane. Generally, heat deposition within the antenna is strongly non-uniform and mostly concentrated at the antenna half facing towards the gap. In particular, the outer antenna ends are only heated via heat conduction and thus reduce the overall temperature in each antenna arm. Interestingly, a minimum for the heat source density also occurs at the upper apex part, even stretching further into the antenna, although the antenna's bottom part is significantly heated.

The corresponding electric field enhancement in the xz-plane is shown in the lower plot in figure 5(b), which is also non-uniform along the antenna thickness. Two pronounced maxima occur at the antenna's top and bottom side and are caused by the sharp tips in that direction. The top one is particularly strong because the field stretches undisturbed into the dielectric, whereas at the bottom the field distribution is changed due to the additional interface resulting from the substrate. Nonetheless, enhancement factors in the order of 10^3 are present in large parts of the gap area along the z-direction.

Figure 5(c) shows the heat source density and the normalized intensity enhancement factor for the same bow-tie antenna as before in the xy-plane. The former exhibits strongly localized maxima at the interface to the surrounding dielectric, which coincide with those observed in the xz-plane and decrease towards the centre line. At both antenna ends no heating occurs, because surface charge is accumulated there, resulting in a decreasing current towards the ends. This is in agreement with previous calculations for currents in bow-tie antennae [38]. On the other hand, the accumulated surface charge leads to the strong field enhancement plotted in the lower image in figure 5(c).

The heat source density varies with the antenna lengths and allows to calculate the temperature increase as well as a damage threshold for each antenna as described in [29].

The respective maximum temperature for antenna lengths between 100 and 180 nm for different incident intensities is plotted in the upper diagram in figure 6. Antennas in the range of the resonance length of approximately 110 nm are damaged at lower incident intensities whereas slightly off-resonant antennae withstand higher intensities. These simulation results also agree with our experimental findings, where we have found regular antenna damage for 140 nm long

antennae at a given intensity and almost no damage for 200 nm long ones. This is understood by looking at the heat source density in the xy-plane, where almost no heating at all occurs at the outer antenna ends. Therefore one can think of the antenna ends as a passive cooler, which reduces the overall temperature increase for longer and antennae. However, the antennae cannot be made arbitrary long since off-resonant antennae lead to a reduced nonlinear signal as shown by Metzger *et al* [39], which would also hamper the generation of EUV radiation.

For HHG, intensities in the order of $10^{13}\,\mathrm{W\,cm^{-2}}$ are required and the harmonic yield ultimately depends on the peak intensity and the volume in which it is present. Therefore, taking thermal damage into account, not only the maximum enhancement has to be considered, but also the maximally possible incident intensity without damaging the antennae. Both quantities are derived by previously introduced calculations. The intensity in the gap centre including enhancement from the nano-antennae as well as the area in the xy-plane with an intensity of at least $3 \times 10^{13}\,\mathrm{W\,cm^{-2}}$, is plotted for different antenna lengths in figure 6. For every length, thermal damage is avoided by choosing the respective maximum incident intensity. Antennas between 140 and 175 nm enable peak intensities higher than $10^{14}\,\mathrm{W\,cm^{-2}}$ with an enhancement area in the xy-plane of more than $1500\,\mathrm{nm^2}$ per antenna. Both the peak intensity and the enhancement area are maximal for a 160 nm long antenna. Taking the accuracy of the manufacturing process into account, antennae between 140 and 175 nm are expected to produce the highest harmonic yield, although being slightly off-resonant but thermally more stable.

Here, we do not calculate the actual HHG spectra and focus on experimental aspects of HHG driven by plasmonic fields. However, it should be noted, that this generation scheme potentially offers exciting perspectives to access the single-atom HHG response; this is an ongoing topic of research (see e.g. [15]) and will be the subject of further investigations.

5. Gas density

As pointed out by Sivis *et al* [17] the gas density and thus the number of atoms in the gap region of the bow-tie antennae is of major importance to understand the origin of the measured EUV radiation. The gas nozzle employed to feed gas onto the sample is therefore characterized with a velocity-map-imaging spectrometer [40]. For the characterization the gas jet propagates freely into vacuum like in well known HHG experimental setups. This allows to assess the number of contributing atoms as accurately as possible and also enables comparisons with cavity enhanced systems as performed by Raschke [19].

Figure 7 shows the sum of approximately hundred single images to reconstruct the gas density in the xy-plane for two different z-positions. The fringes present in figure 7(b) are caused by a varying overlap of the underlying single images for a constant step size in both dimensions. Nonetheless, the resulting gas jet with its spatial distribution is clearly visible with a nearly circular shape. For larger separations from the nozzle, the gas density drops significantly as expected.

For each z-position the full width at half maximum (FWHM) is determined in x- and y-direction, grouped and fitted with a linear function. The intersection of these fit curves then reveals the previously unknown nozzle position. Both the fit curves and the gas density at different z-positions are plotted in figure 7 to illustrate the gas density behind the nozzle. From the fit data a divergence angle of 33° is obtained. In combination with the mass flow controller the number of atoms at the sample is now accessible. In our experiments typical distances

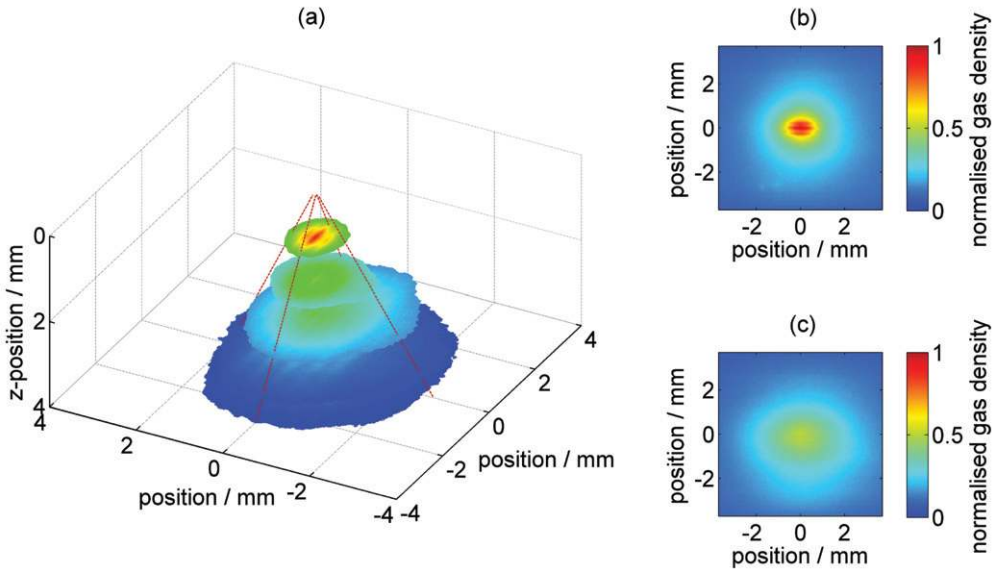

Figure 7. (a) Three dimensional representation of the gas density. The edge of the gas jet is set to the FWHM for each measurement. The dashed lines show a linear fit of the calculated widths from which a divergence angle of 33° is obtained. (b), (c) Reconstructed gas density behind the nozzle for two different distances. Approximately hundred images are used for the reconstruction at each distance. A varying overlap between individual images causes the fringes present in (b). (c) A reduced gas density is clearly seen for larger distances.

between the sample and the gas nozzle are in the order of 100 μm and the measured mass flow is 0.175 sccm (measured with a MKS 647C controller), which is approximately 1.7×10^{-5} g s^{-1}. Hence, the gas density at the sample is in the order of 7.4×10^{-2} atoms nm^{-3}. Furthermore, for a 50 nm thick bow-tie antenna with a gap size of 20 nm the conservatively estimated interaction volume is $20 \times 50 \times 40$ nm leading to 2.9×10^{3} atoms in it. Since roughly 200 antennae are illuminated with the laser pulse, in total 5.9×10^{5} atoms contribute to the measured signal.

Kim *et al* [32] on the other hand, report $\sim 8 \times 10^{4}$ gas atoms in the interaction volume, which is almost an order of magnitude lower compared to our experimental conditions.

6. Spectra

In figure 8, exemplary spectra for 200 nm bow-tie antennae are plotted with figure 8(a) covering a broader spectral range in the EUV and figure 8(b) showing a detail scan around 90 nm. For both spectra xenon gas with a backing pressure of 200 mbar was fed onto the sample and the nozzle position has been optimized. Xenon gas is chosen due to its higher harmonic efficiency in comparison with other noble gases. Also the current photon flux does not allow us to switch to argon or helium gas to achieve higher cut-off energies. The nozzle is identical to the one characterized in section 5. Grey background shading indicates the harmonic orders of the driving laser and orange lines represent xenon plasma lines and their relative intensities [41]. Most strikingly, high photon numbers are detected between 100 and 110 nm, which is attributed to

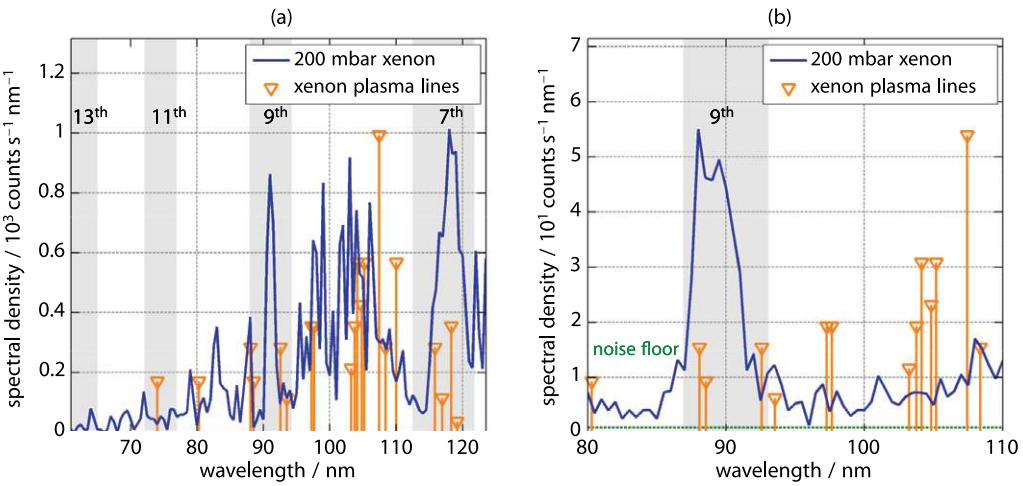

Figure 8. Measured spectra in xenon with 200 nm bow-tie antennae at a backing pressure of 200 mbar. Grey background shading indicates harmonic orders of the driving laser, whereas orange lines represent xenon plasma lines and their respective relative intensities. (a) Measured spectrum in xenon with 200 mbar backing pressure. Radiation from multiple plasma lines is found around 104 nm. (b) Detail scan between 80 and 110 nm at a central wavelength of 810 nm (spectrum is not efficiency corrected). Surprisingly, contributions from multiple plasma lines around 104 nm do not show up like in (a).

multiple plasma lines in this spectral range. A pronounced peak with the highest photon numbers is found at 117 nm, where only four plasma lines can contribute to the total signal. Taking the relative intensities into account and comparing the photon numbers with those at 104 nm a lower signal is expected if plasma radiation alone is its source. Another spectral peak coincides with the spectral position of the ninth harmonic at 91 nm. However, the spectral width is smaller than expected for the harmonic radiation.

Figure 8(b) was measured with the grating with a design wavelength from 110 to 310 nm due to alignment purposes. Therefore, no diffraction efficiency is known for the spectral range below 110 nm and the spectrum in figure 8(b) has not been corrected for it. Also note, that the central wavelength is slightly shifted to 810 nm. The dashed green line indicates the noise floor caused by dark counts from the electron multiplier. Interestingly no plasma line contributions for wavelengths larger than 95 nm are found in the spectrum. However, a pronounced peak at 90 nm is present, which does not directly coincide with xenon plasma lines.

Additional spectra were taken under identical conditions as before with 170 nm antennae to maximize the electric field enhancement as pointed out in section 4. The central laser wavelength is 820 nm and figure 9 shows an efficiency corrected spectrum in the range between 50 and 120 nm to check for higher harmonic orders. As before, significant photon numbers are detected around 104 nm, which result from discrete transitions in single-ionized xenon [41]. Surprisingly few photons are measured at 117 nm, though. The highest photon numbers are found at 76 nm, which is close to the spectral position of the eleventh harmonic. Slightly less signal is present at 91 nm, i.e. at the spectral position of the ninth harmonic order.

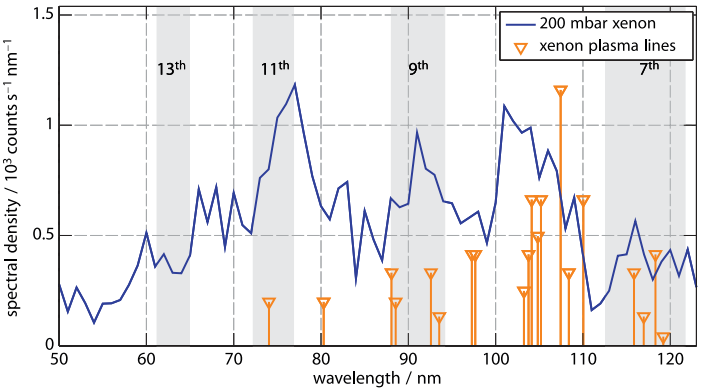

Figure 9. Measured spectra in xenon with 170 nm long bow-tie antennae at a backing pressure of 200 mbar. Again, radiation from multiple plasma lines is found around 104 nm, but surprisingly few photons are detected around 117 nm. The highest photon numbers occur at 76 nm, which is close to the eleventh harmonic of the driving laser.

7. Summary and outlook

In summary, we have presented an analysis of important parameters influencing the generation of EUV radiation utilizing the plasmonic field enhancement of bow-tie optical antennae. A damage threshold for the antenna is experimentally found and explained by a simple theoretical model, which facilitates to find thermally stable antennae. Based on the ion imaging technique with a velocity map imaging spectrometer, the gas nozzle employed in the experiments was thoroughly characterized to determine the gas density at the sample as accurately as possible. The spectra obtained with FIB-produced nano-antennae are all in contrast to data reported by Kim *et al* [5], who reported the observation of harmonic radiation alone without additional lines resulting from plasma radiation in an identical experiment. They are however in agreement with early experiments on HHG with peak intensities of 3×10^3 W cm^{-2}, where contributions from neutral and single-ionized xenon to the spectra have been found [30, 42]. These intensities are well within reach in the feed gap of the nano-antennae and ALE as an incoherent process is likely to occur. This is supported by the observed changes to the sapphire substrate, which require peak intensities of at least 1×10^{13} W cm^{-2} as outlined in section 3 in order to appear. An insufficient field enhancement from the nano-antennae as a possible source of error is therefore highly unlikely. Moreover, ALE alone has been found in independent experiments on HHG in the presence of optical antennae, which further confirms the measured spectra [17]. Recently Park *et al* [18] also reported to have found ALE in their EUV spectra.

In order to distinguish between ALE or harmonic generation as a source for the measured EUV radiation additional measurements are necessary. The coherence properties of the bow-tie emitted radiation reveal information on the source of the measured radiation since HHG as a coherent process should exhibit a well defined beam profile. ALE in contrast is an incoherent process and thus no beam profile is expected. Secondly, by switching to a different driving wavelength of e.g. 1064 nm ALE contributions and harmonics of the driving laser would spectrally be well separated and thus enable an unambiguous determination of its source. An increased driving wavelength would be advantageous in even more aspects. The structuring precision requirements are eased due to larger structure sizes, the damage threshold is increased

because of a reduced absorption in the gold layer and larger antenna sizes, and finally the HHG cut-off is increased at the expense of conversion efficiency.

Acknowledgments

This work was funded by Deutsche Forschungsgemeinschaft within the Cluster of Excellence QUEST, Centre for Quantum Engineering and Space-Time Research. We furthermore acknowledge support by Deutsche Forschungsgemeinschaft and Open Access Publishing Fund of Leibniz Universität Hannover.

Note added in proof. During the review process we became aware of the following paper dealing with the same experimental scheme [43].

References

[1] Mühlschlegel P, Eisler H-J, Martin O J F, Hecht B and Pohl D W 2005 Resonant optical antennas *Science* **308** 1607–9

[2] Schuller J A, Barnard E S, Cai W, Jun Y C, White J S and Brongersma M L 2010 Plasmonics for extreme light concentration and manipulation *Nature Mater.* **9** 193–204

[3] Hanke T, Krauss G, Träutlein D, Wild B, Bratschitsch R and Leitenstorfer A 2009 Efficient nonlinear light emission of single gold optical antennas driven by few-cycle near-infrared pulses *Phys. Rev. Lett.* **103** 257404

[4] Hanke T, Cesar J, Knittel V, Trügler A, Hohenester U, Leitenstorfer A and Bratschitsch R 2012 Tailoring spatiotemporal light confinement in single plasmonic nanoantennas *Nano Lett.* **12** 992–6

[5] Kim S, Jin J, Kim Y-J, Park I-Y, Kim Y and Kim S-W 2008 High-harmonic generation by resonant plasmon field enhancement *Nature* **453** 757–60

[6] Krausz F and Ivanov M 2009 Attosecond physics *Rev. Mod. Phys.* **81** 163–234

[7] Sansone G, Kelkensberg F, Morales F, Perez-Torres J F, Martin F and Vrakking M J J 2012 Attosecond time-resolved electron dynamics in the hydrogen molecule *IEEE J. Sel. Top. Quantum Electron.* **18** 520–30

[8] Udem Th, Holzwarth R and Hänsch T W 2002 Optical frequency metrology *Nature* **416** 233–7

[9] Cingoz A, Yost D C, Allison T K, Ruehl A, Fermann M E, Hartl I and Ye J 2012 Direct frequency comb spectroscopy in the extreme ultraviolet *Nature* **482** 68–71

[10] Gohle C, Udem T, Herrmann M, Rauschenberger J, Holzwarth R, Schuessler H A, Krausz F and Hänsch T W 2005 A frequency comb in the extreme ultraviolet *Nature* **436** 234–7

[11] Jones R J, Moll K D, Thorpe M J and Ye J 2005 Phase-coherent frequency combs in the vacuum ultraviolet via high-harmonic generation inside a femtosecond enhancement cavity *Phys. Rev. Lett.* **94** 193201

[12] Ozawa A *et al* 2008 High harmonic frequency combs for high resolution spectroscopy *Phys. Rev. Lett.* **100** 253901

[13] Yost D C, Schibli T R, Ye J, Tate J L, Hostetter J, Gaarde M B and Schafer K J 2009 Vacuum-ultraviolet frequency combs from below-threshold harmonics *Nature Phys.* **5** 815–20

[14] Husakou A, Im S-J and Herrmann J 2011 Theory of plasmon-enhanced high-order harmonic generation in the vicinity of metal nanostructures in noble gases *Phys. Rev.* A **83** 043839

[15] Ciappina M F, Biegert J, Quidant R and Lewenstein M 2012 High-order-harmonic generation from inhomogeneous fields *Phys. Rev.* A **85** 033828

[16] Yang Y-Y *et al* 2013 High-harmonic and single attosecond pulse generation using plasmonic field enhancement in ordered arrays of gold nanoparticles with chirped laser pulses *Opt. Express* **21** 2195–205

[17] Sivis M, Duwe M, Abel B and Ropers C 2012 Nanostructure-enhanced atomic line emission *Nature* **485** E1–3

[18] Park I-Y, Choi J, Lee D-H, Han S, Kim S and Kim S-W 2013 Generation of EUV radiation by plasmonic field enhancement using nano-structured bowties and funnel-waveguides *Ann. Phys.* **525** 87–96

[19] Raschke M B 2013 High-harmonic generation with plasmonics: feasible or unphysical? *Ann. Phys.* **525** A40–2
[20] Yavuz I, Bleda E A, Altun Z and Topcu T 2012 Generation of a broadband XUV continuum in high-order-harmonic generation by spatially inhomogeneous fields *Phys. Rev.* A **85** 013416
[21] Ciappina M F, Aćimović S S, Shaaran T, Biegert J, Quidant R and Lewenstein M 2012 Enhancement of high harmonic generation by confining electron motion in plasmonic nanostrutures *Opt. Express* **20** 26261–74
[22] Shaaran T, Ciappina M F and Lewenstein M 2012 Quantum-orbit analysis of high-order-harmonic generation by resonant plasmon field enhancement *Phys. Rev.* A **86** 023408
[23] Shaaran T, Ciappina M F and Lewenstein M 2012 Estimating the plasmonic field enhancement using high-order harmonic generation: the role of the field inhomogeneity *J. Mod. Opt.* **59** 1634–9
[24] Pérez-Hernández J A, Ciappina M F, Lewenstein M, Roso L and Zaïr A 2013 Beyond carbon *k*-edge harmonic emission using a spatial and temporal synthesized laser field *Phys. Rev. Lett.* **110** 053001
[25] Yavuz I 2013 Gas population effects in harmonic emission by plasmonic fields *Phys. Rev.* A **87** 053815
[26] Ciappina M F, Shaaran T and Lewenstein M 2013 High order harmonic generation in noble gases using plasmonic field enhancement *Ann. Phys.* **525** 97–106
[27] Fetić B, Kalajdžić K and Milošević D B 2013 High-order harmonic generation by a spatially inhomogeneous field *Ann. Phys.* **525** 107–17
[28] Luo J, Li Y, Wang Z, Zhang Q and Lu P 2013 Ultra-short isolated attosecond emission in mid-infrared inhomogeneous fields without CEP stabilization *J. Phys. B: At. Mol. Opt. Phys.* **46** 145602
[29] Pfullmann N, Waltermann C, Kovačev M, Knittel V, Bratschitsch R, Akemeier D, Hütten A, Leitenstorfer A and Morgner U 2013 Nano-antenna-assisted harmonic generation *Appl. Phys.* B 1–5
[30] Li X F, L'Huillier A, Ferray M, Lompré L A and Mainfray G 1989 Multiple-harmonic generation in rare gases at high laser intensity *Phys. Rev.* A **39** 5751–61
[31] Lindner F, Stremme W, Schätzel M G, Grasbon F, Paulus G G, Walther H, Hartmann R and Strüder L 2003 High-order harmonic generation at a repetition rate of 100 khz *Phys. Rev.* A **68** 013814
[32] Kim S *et al* 2012 Reply *Nature* **485** E1–3
[33] Wang J, Chen Y, Chen X, Hao J, Yan M and Qiu M 2011 Photothermal reshaping of gold nanoparticles in a plasmonic absorber *Opt. Express* **19** 14726–34
[34] von der Linde D and Schüler H 1996 Breakdown threshold and plasma formation in femtosecond laser–solid interaction *J. Opt. Soc. Am.* B **13** 216–22
[35] Oskooi A F, Roundy D, Ibanescu M, Bermel P, Joannopoulos J D and Johnson S G 2010 Meep: a flexible free-software package for electromagnetic simulations by the FDTD method *Comput. Phys. Commun.* **181** 687–702
[36] Rakic A D, Djurišic A B, Elazar J M and Majewski M L 1998 Optical properties of metallic films for vertical-cavity optoelectronic devices *Appl. Opt.* **37** 5271–83
[37] Baffou G, Girard C and Quidant R 2010 Mapping heat origin in plasmonic structures *Phys. Rev. Lett.* **104** 136805
[38] Crozier K B, Sundaramurthy A, Kino G S and Quate C F 2003 Optical antennas: resonators for local field enhancement *J. Appl. Phys.* **94** 4632–42
[39] Metzger B, Hentschel M, Lippitz M and Giessen H 2012 Third-harmonic spectroscopy and modeling of the nonlinear response of plasmonic nanoantennas *Opt. Lett.* **37** 4741–3
[40] Eppink A T J B and Parker D H 1997 Velocity map imaging of ions and electrons using electrostatic lenses: application in photoelectron and photofragment ion imaging of molecular oxygen *Rev. Sci. Instrum.* **68** 3477–84
[41] Sansonetti J E and Martin W C 2005 Handbook of basic atomic spectroscopic data *J. Phys. Chem. Ref. Data* **34** 1559–2259
[42] L'Huillier A, Schafer K J and Kulander K C 1991 Theoretical aspects of intense field harmonic generation *J. Phys. B: At. Mol. Opt. Phys.* **24** 3315
[43] Sivis M, Duwe M, Abel B and Ropers C 2013 Extreme-ultraviolet light generation in plasmonic nanostructures *Nature Phys.* **9** 304–9